QUANTITATIVE AND QUALITATIVE ASSESSMENT OF AS-CAST MICROSTRUCTURE AND MICROPOROSITY OF γ-γ′ Co-BASED SUPERALLOYS

Damian Migas, Stanisław Roskosz and Grzegorz Moskal
Department of Materials Technologies, Silesian University of Technology, Krasińskiego 8 str., 40-019 Katowice, Poland

https://doi.org/10.1007/s40962-022-00918-2

Abstract

The γ-γ′ Co-based alloys have attracted extensive attention as a new class of materials for high temperature applications. The work is focused on quantitative and qualitative microstructural characterization of selected γ-γ′ type Co-based superalloys obtained by gravity casting. The four Co-based alloys were prepared via vacuum induction melting. The microstructure was analyzed by means of light microscopy and scanning electron microscopy. The microstructural parameters such as porosity and secondary dendrite arm spacing (SDAS) were evaluated by image analysis. The new Co-based superalloys are characterized by proper as-cast microstructure owing to low SDAS and limited microporosity. The values of secondary dendrite arm spacing are comparable for all alloys. The W-free alloys containing Mo and Nb exhibit substantially lower shrinkage porosity compared to those of Co–Al–W and Co–Ni–Al–W. Due to crystallization of Mo and Nb rich phases at lower temperatures, these alloys are characterized by higher solidification range.

Keywords: *cobalt-based superalloys, electron microscopy, SDAS, microporosity, W-free alloys*

Introduction

The novel γ-γ′ Co-based superalloys have gained attention of investigators since discovery of Sato et al.[1] The newly developed alloys are promising structural materials for aero-engine blades. The high temperature strength of the alloys may be substantially optimized due to efficient strengthening mechanism, which was not available in the case of conventional Co-based superalloys.[2,3]

The microstructure of new Co-based alloys is composed of γ–Co_{ss} (Co solid solution), and cuboidal and coherent γ′–Co_3(Al, W) precipitates.[1,4,5] The base alloy exhibiting γ-γ′ microstructure was Co–9Al–9W (at. %), whereas presence of the desirable double-phase microstructure was reported also in the case of alloys other than ternary.[6,7] Furthermore, formation of γ′ phase was noticed in Co-based systems other than Co–Al–W.[8–11] Therefore, there are many possibilities to create γ-γ′ microstructure of novel Co-based alloys. Numerous authors describe as heat-treated microstructure of new cobalt superalloys.[12,13] Moreover, the articles which describe as-cast microstructure of alloys are also available.[14–16] Considering fabrication of γ-γ′ Co-based superalloys, the investigators are often focused on microsegregation, partition coefficient, solidification path and other.[17–19] In most of cases, the microstructural analysis is qualitative. However, the information about new class of superalloys could be supplemented with data concerning quantitative description of microstructure.

Analyzed alloys belong to a new group of cobalt-based materials reinforced with Co_3(Al, X) phase with properties like γ′ phase in nickel superalloys and Ni_3Al formula. The production of a Co_3(Al, X) type coherent reinforcing phase requires the addition of, among others, components such as tungsten, as well as molybdenum and niobium. This allows to produce alloys based on a cobalt solid solution matrix strengthened by heat treatment with Co_3(Al, W) and Co_3(Al, Mo, Nb) phases for tungsten based and tungsten-free alloys, respectively. In the case of tungsten-free alloys, it is necessary to introduce both components: molybdenum and niobium, because so far it has not been possible to confirm the presence of Co_3Mo and Co_3Nb phases with $L1_2$ lattice, but only in the $D0_{19}$ form. Moreover, the introduction of Mo and Nb instead of W lowers the density

Received: 08 March 2022 / Accepted: 02 November 2022 /
Published online: 5 December 2022

of the alloys, which is an important exploitation factor. The introduction of nickel, in turn, increases the equilibrium range of the $L1_2$ phase and increases its thermal stability. It also increases the temperature of the $L1_2$ phase solvus, which improves the heat resistance of these alloys and increases the operating temperature.

Additions of the Ni, Mo and Nb alloying elements are among the most used in the new type of cobalt superalloys.[20–26] Typically, for this type of alloys, treatment consisting in homogenization and supersaturation or only supersaturation at a temperature range of 1250–1300 °C for up to 24 hours with cooling in water, followed by late supersaturation in the range of the solvus temperature of the $L1_2$ phase, i.e., 900–1000 °C.[27–29]

In the study, we analyze qualitatively and quantitatively the γ-γ′ type Co-based alloys. For this purpose, different ternary, quaternary and quinary alloys were prepared, including two γ′-Co_3(Al, W) forming alloys and two W-free ones. The analysis included assessment of gas and shrinkage microporosity, which is typical defect in as-cast superalloys. Excessive pores fraction may invariably degrade mechanical properties of superalloys castings. Furthermore, secondary dendrite arm spacing (SDAS) was investigated. The representative results as well as assessment procedures are provided.

Experimental Methods

Preparation of Alloys

The alloys chosen for investigation were Co–9Al–9W, Co–20Ni–7Al–7W, Co–10Al–5Mo–2Nb and Co–20Ni–10Al–5Mo–2Nb (at. %). The alloys were prepared by vacuum induction melting (VIM) technique. The raw metals were melted in alumina crucible at temperature over 1600 °C for approx. 5 minutes. Subsequently, the molten metal was casted at ca. 1600 °C to previously prepared graphite mold. The obtained cylindrical ingots are measured as ∅18 × 150 mm. The experimentally measured composition of alloys may be seen in Table 1. The microstructural characterization was based on observation of three characteristic zones of ingot: A, B, C (Figure 1). The observations were made on surfaces perpendicular to the ingot axis.

The observations and measurements were carried out using light microscope and scanning electron microscope (SEM) equipped with the energy dispersion spectrometer (EDS). The average chemical composition of alloys was measured by ICP-OES (inductively coupled plasma optical emission spectrometer) method.

To measure porosity in each zone of ingot, ten random images of porosity were recorded by light microscopy (bright field technique) at a magnification of 200×. It is important to differentiate gas and shrinkage pores and their selective measurement. The porosity assessment was performed by the ImageJ software, using porosity macroinstruction. The instruction enables selective measurement of gas and shrinkage porosity basing on the dimensionless shape factor (ξ),

$$\xi = \frac{4\pi A}{P^2} \qquad \text{Eqn. 1}$$

where A is the flat cross-sectional area, and P - the flat cross-sectional perimeter. To classify detected pores as gas (Figure 2c) or shrinkage (Figure 2d) porosity, the value of the dimensionless shape factor (0.8) was taken as a criterion.[30]

The stereological parameter λ_0 was used to describe the distance between secondary dendrite arms. The λ_0 can be defined as the distance between centers of two consecutive dendrite arms. The actual distance between dendrite arms is based on measurements made on flat metallographic specimens. Although longitudinal metallographic samples are from the axis of the casting, the secondary dendrite arms may be oriented perpendicular to the plane of the landing. Moreover, the plane of metallographic sample may by not parallel to the axis of the main arms. Therefore, the so-called apparent distance λ_a or random λ_r between the dendrite arms is measured (Figure 2e). In the case of binary images of the secondary dendrite arms, the incisor perpendicular to the secondary arms is projected by measuring the apparent distance λa as the distance between the points

Table 1. Measured Chemical Composition of Castings

Analyzed alloys	Measured chemical composition (ICP-OES) in wt %					
	Al–K	Co–K	Ni–K	W–M	Mo–L	Nb–L
Co–9Al–9W	4.02	Bal.	–	24.55	–	–
Co–20Ni–7Al–7W	2.85	Bal.	18.36	20.02	–	–
Co–10Al–5Mo–2Nb	4.32	Bal.	–	–	8.39	3.02
Co–20Ni–10Al–5Mo–2Nb	4.11	Bal.	20.95	–	8.45	3.11

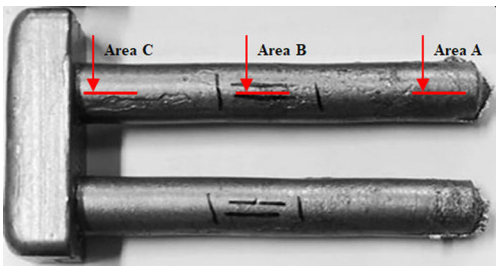

Figure 1. Macrograph of single casting with marked areas of sampling.

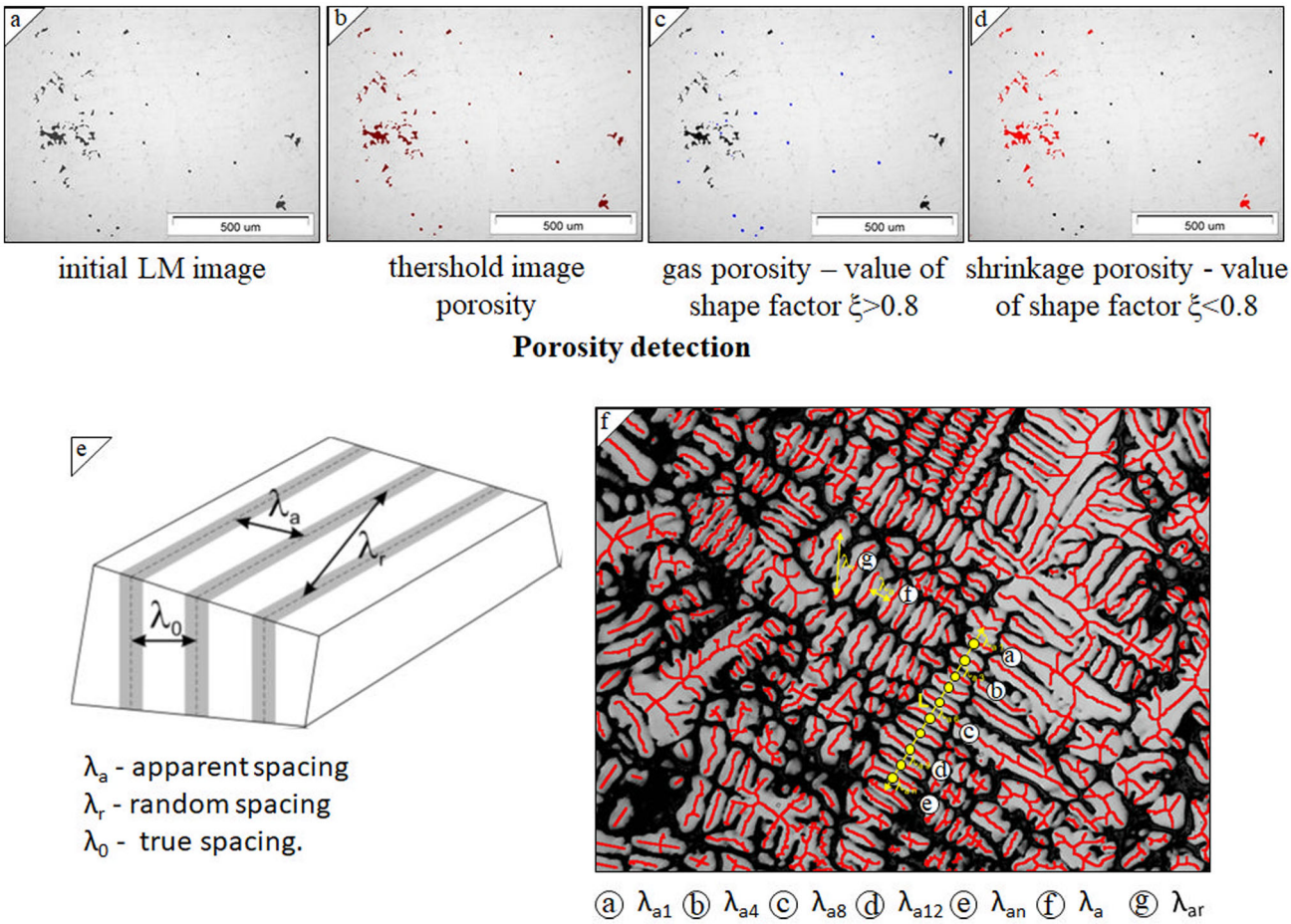

Figure 2. Schematic of microporosty and SDAS assessment.

of intersection of these lines with the dendrite arms (Figure 2f). In this case, the average real distance between the arms can be determined from the formula:

$$\lambda_0 = \frac{\pi}{4}\lambda_a = \frac{\pi}{4}\frac{L}{N-1} \qquad \text{Eqn. 2}$$

where L–the length of the incisor perpendicular to the secondary arms [μm], N–the number of intersections with the secondary dendrite arms.

Taking into consideration that

$$\lambda_0 = \frac{\pi}{4}\lambda_a \qquad \text{Eqn. 3}$$

partial results (λ_{a1} do λ_{an}) allow for determination of SDAS distribution (Figure 2f). The schematic of porosity and SDAS detection using image analysis is shown in Figure 2.

The microstructural analysis was performed on etched and polished samples. In the case of non-etched ones, specimens for microstructure evaluation were prepared by grinding, polishing and chemical etching. A reagent containing 60ml HCl, 20 ml HNO_3, 20 ml CH_3COOH was used for etching of samples. The light microscopy (LM) images were acquired by the Nikon Eclipse MA200 microscope.

Results and Discussion

The first part of investigation concerned quantitative evaluation of as-cast microstructure. Figure 3 shows example micrographs presenting primary microstructure of all investigated Co-based alloys. All materials are characterized by dendritic microstructure, whereas the main differences between the studied alloys may be found in dendrite arms spacing.

The results concerning characterization od SDAS of four as-cast Co-based superalloys are shown in Figure 4. and Table 2. Taking into consideration the average SDAS related to all zones, the microstructure of alloys is similar. The difference in average dendrite arm spacing is no more than 2 μm. For all alloys, the highest value of SDAS was measured in zone C, which is attributed to the lowest

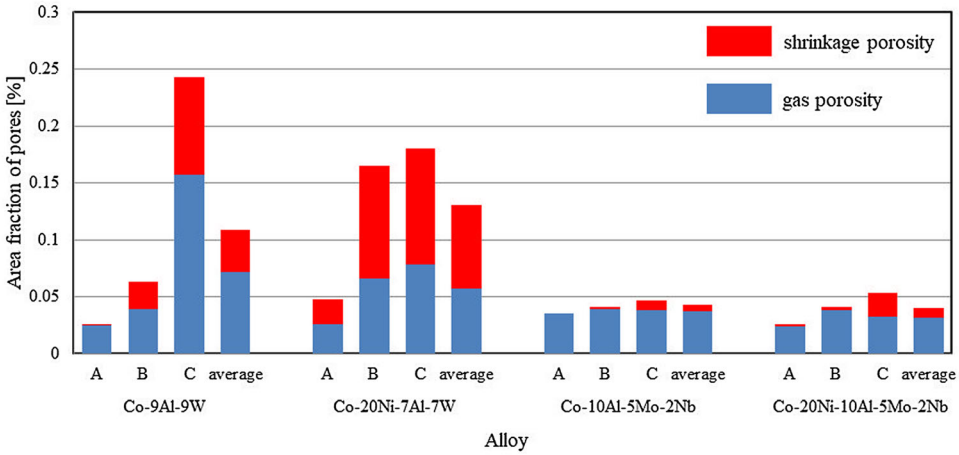

Figure 3. Average values of porosity in different ingot areas.

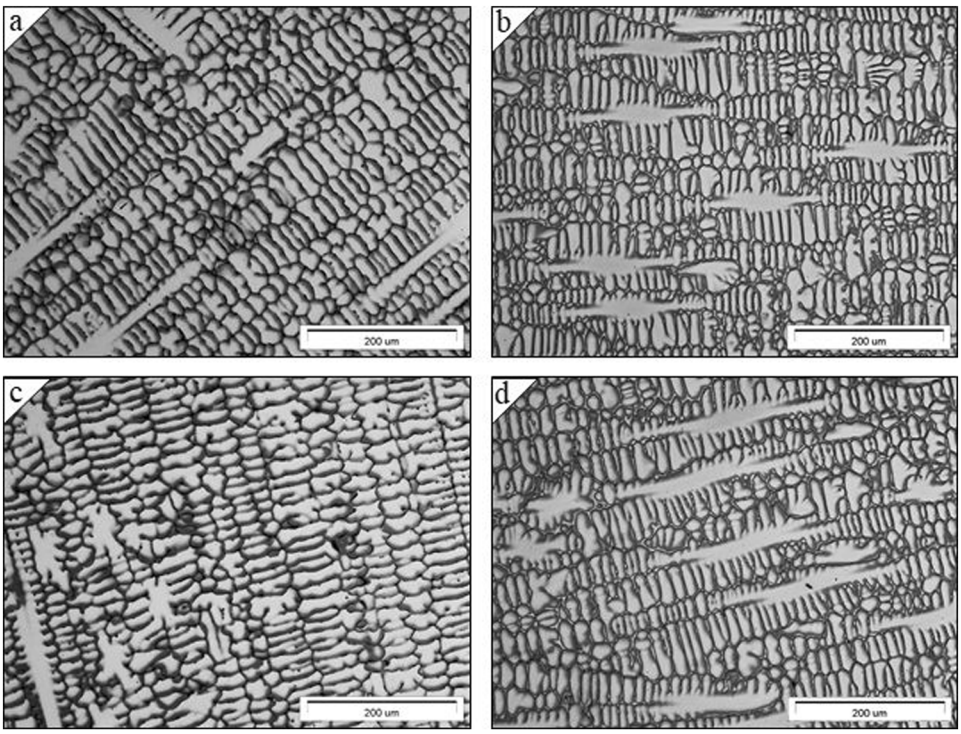

Figure 4. Example micrographs of dendritic structures of Co-based superalloys; (a) Co–9Al–9W; (b) Co–20Ni–7Al–7W; (c) Co–10Al–5Mo–2Nb; (d) Co–20Ni–10Al–5Mo–2Nb.

solidification rate in the upper part of ingot. However, the difference between SDAS measured in zone A and C was less than 3 μm. The highest SDAS was reported for Co–9Al–9W alloy.

The distribution of SDAS within different zones of ingots is shown in Figure 5. In the case of Co–9Al–9W alloy, most of detected SDAS were in the range 8–12 μm in A and B zone. For zone A, SDAS values are mostly between 5 and 9 μm. The similar observation may be done for the SDAS distribution in the case of Co–20Ni–7Al–7W alloy. For Co–20Ni–5Al–5Mo–2Nb alloy, secondary dendrite arm spacings are mostly in the range 2.5–9.4 μm (zones A and B). The analogous distribution may be observed for zone A of Co-20Ni-10Al-5Mo-2Nb, however, the SDAS values for this alloy in zones B and C are rather uniformly distributed. The SDAS distribution in zone C of Co–10Al–5Mo–2Nb is more uniform compared to that of zones A and B of the same alloy.

The results of porosity measurements are shown in Figure 6 and Table 3. The highest gas porosity was detected for Co–9Al–9W alloy, especially in zone C. Slightly lower porosity was observed in the case of Co–20Ni–7Al–7W

Table 2. Results of Secondary Arm Dendrite Spacing Assessment

Alloy	SDAS								
	A			B			C		
	$\bar{x}$ [μm]	σ [μm]	CV [%]	$\bar{x}$ [μm]	σ [μm]	CV [%]	$\bar{x}$ [μm]	σ [μm]	CV [%]
Co-9Al-9W	7.73	2.13	27.5	9.57	2.34	24.5	10	2.6	26
Co-20Ni-7Al-7W	7.63	2.37	31	7.67	2.73	35.6	8.92	2.95	33.1
Co-10Al-5Mo-2Nb	6.67	2.87	43	6.73	3.4	50.5	7.87	3.41	43.3
Co-20Ni-10Al-5Mo-2Nb	7.06	2.88	40.8	7.69	5.31	69.1	8.84	3.13	35.4

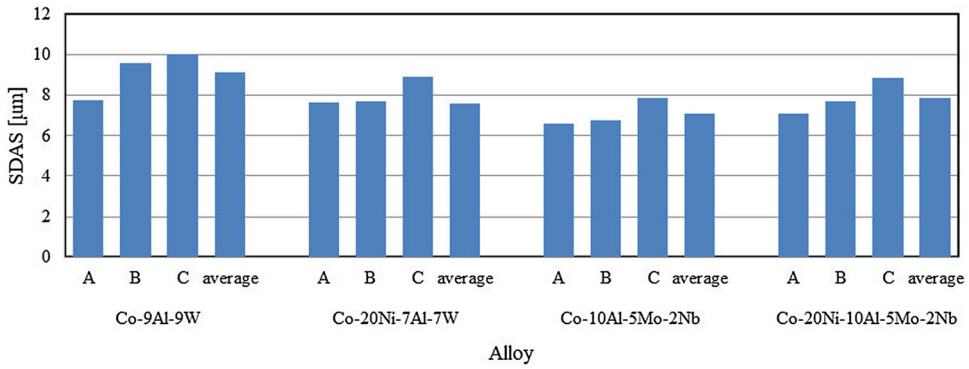

Figure 5. Average values of SDAS in different ingot areas.

alloy. The lowest content of gas pores was detected in W-free Co–10Al–5Mo–2Nb and Co-20Ni–10Al–5Mo–2Nb. The W-containing alloys are characterized by presence of shrinkage porosity, which is concentrated mostly in upper parts of ingot. The W-free alloys were characterized by substantially lower shrinkage porosity compared to that of Co–Al–W and Co–Ni–Al–W alloys. For all investigated metallic materials, the total porosity was highest in the top zone of ingot. During the presented research, efforts were made to maintain the laminar flow conditions of liquid metal, with particular emphasis on avoiding the effect of turbulence. For this reason, the flow conditions in all analyzed variants were assumed to be very similar and it was assumed that the speed of the metal stream did not affect the formation of gas pores. Therefore, this issue was not considered in further comments.

The difference between these group of alloys may be found in crystallization behavior. Therefore, it is worth to observe DTA cooling plots of two representative alloys Co–9Al–9W and Co–10Al–5Mo–2Nb (Figure 7). Both curves show great endothermic effects. The onset of those peaks is corresponding to *liquidus* temperature. The main difference is that the crystallization peak of W-free alloy is substantially wider, which implies higher solidification range. Moreover, the second endothermic effect may be observed at 1250 °C. This small peak may be corresponding to crystallization of other phase constituents, which are supposed to form due to partition of Mo and Nb to interdendritic spaces. Due to limited segregation, Co–Al–W and Co–Ni–Al–W alloys are characterized by relatively narrow solidification range, which results in crystallization of γ-$Co_{ss.}$ Solidification of Mo and Nb-containing alloys results in formation of solid solution and intermetallic phases, which substantially widen solidification range and shifts crystallization end to lower temperatures. These observations may be reflected in microstructure.

Figure 8 shows SEM micrographs of the as-cast alloys by BSE mode. The SEM image corresponding to Co–9Al–9W (Figure 8a) reveals typical as-cast microstructure for this alloy.[31] The similar dendritic structure was observed in the case of Co–20Ni–9Al–9W (Figure 8b). These alloys are characterized by limited segregation, which may be seen in distribution of elements (Figure 8e). Therefore, crystallization of those alloys occurs in narrow solidification range and results in dendritic microstructure composed of γ-Co_{ss} dendrites and interdendritic areas. The opposite case was reported for W-free alloys (Figure 8c-d). Although these alloys also exhibit dendritic microstructure, the segregation is more pronounced (Figure 8f). Furthermore, small phases which morphology typical for eutectics were observed. These phases are known as topologically close-packed (TCP) phases with formula Co_3(Mo, Nb).[32] The discussed phase constituents are characterized by $D0_{19}$ structure, and their melting occur at temperatures lower than melting of Co_{ss}.[29] Ni may easily segregate to this type of phase.[33] On the other hand, Davydov et al. reported formation of Laves phases with composition AB_2 in as heat-treated Co–Al–Mo–Nb alloys.[34] Presence of phase

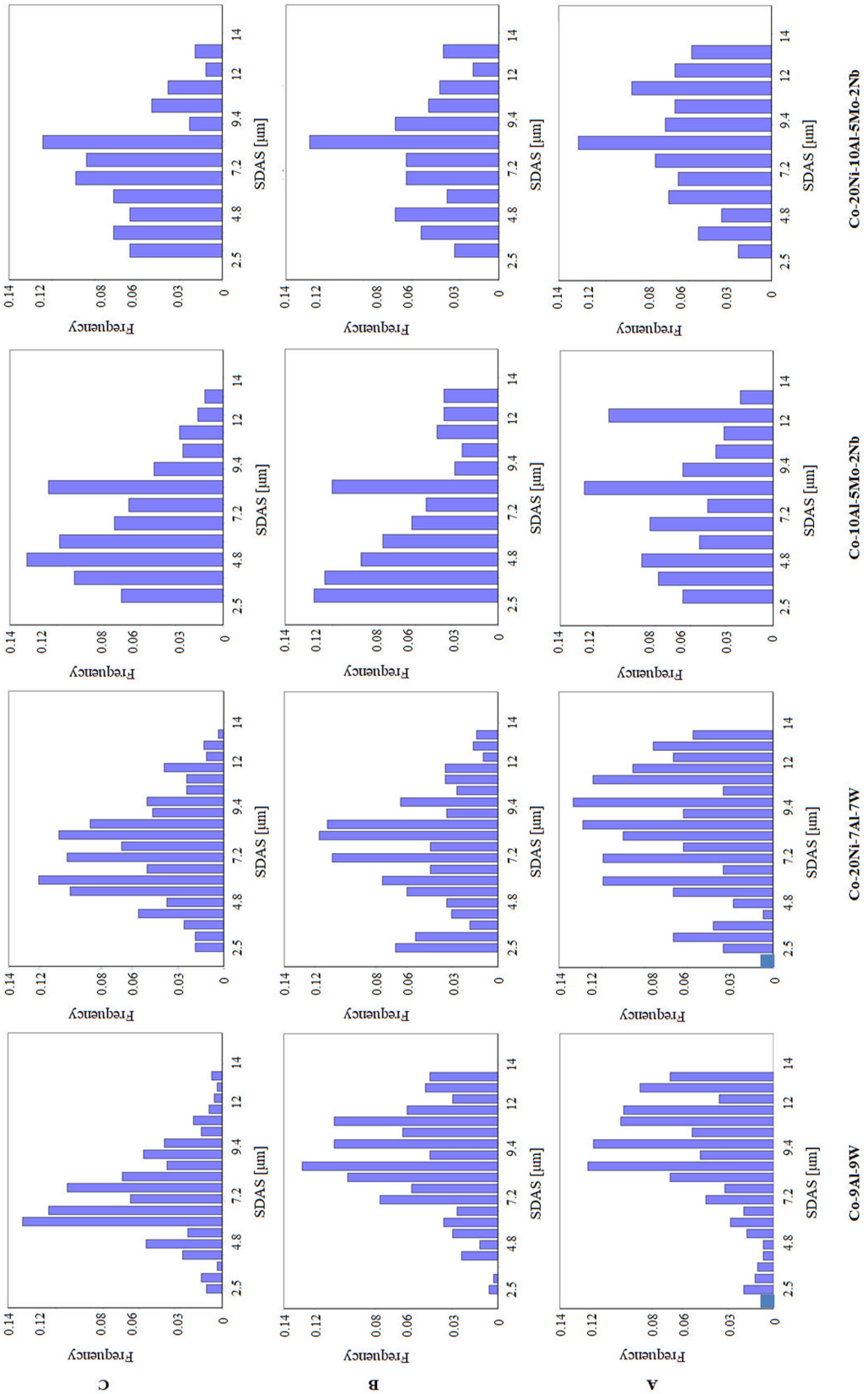

Figure 6. Distribution of SDAS in different ingot areas of the alloys.

Table 3. Results of Microporosity Assessment

Quantitative parameter	Zone of ingot			
	A	B	C	Average
Co-9Al-9W				
Total porosity [%]	0.026	0.063	0.243	0.111
gas porosity [%]	0.025	0.035	0.157	0.072
Shrinkage porosity [%]	0.001	0.024	0.086	0.037
Co-20Ni-7Al-7W				
Total porosity [%]	0.048	0.165	0.180	0.131
gas porosity [%]	0.026	0.066	0.078	0.057
Shrinkage porosity [%]	0.022	0.099	0.102	0.074
Co-10Al-5Mo-2Nb				
Total porosity [%]	0.035	0.041	0.047	0.041
gas porosity [%]	0.035	0.039	0.038	0.037
Shrinkage porosity [%]	–	0.002	0.009	0.006
Co-20Ni-10Al-5Mo-2Nb				
Total porosity [%]	0.026	0.041	0.053	0.040
gas porosity [%]	0.024	0.038	0.033	0.032
Shrinkage porosity [%]	0.002	0.003	0.020	0.008

types such as $D0_{19}$ or Laves is detrimental due to their structure. Moreover, Mo and Nb rich precipitates may decrease in alloy's melting temperature. Solution heat treatment allows for dissolution of the eutectics. However, formation of these phase during crystallization substantially affects solidification range of the alloys. In the case of Co–9Al–9W and Co–20Ni–7Al–7W alloys, crystallization of liquid phase in interdendritic spaces occur at temperature slightly lower than that of dendrite cores. Thus, the crystallization is rapid. For W-free alloys, interdendritic spaces stay longer in liquid state compared to that of W-containing alloys due to substantially higher difference between start and finish od crystallization. Although differences in microporosity are observable, the content of micropores is acceptable for all alloys.

An important factor from the point of view of the segregation of the chemical composition and the formation of individual phases, especially in the interdendritic regions, is also the mobility of alloying elements in the fcc-Co solid solution–Co_{ss}. The literature data indicate that tungsten and niobium will have the lowest diffusion tendency in the Co_{ss} (activation energy 289.2 and 262.0 kJ/mol, respectively, and the frequency factor $D_0 = 5.6 \times 10^{-5}$ and $D_0 = 2.0 \times 10^{-5}$ m^2/s), in the case of aluminum, these values are, respectively, 281.1 kJ/mol and 3.6×10^{-4} m^2/s, and for niobium 305.2 kJ/mol and 2.8×10^{-3} m^2/s. This indicates the highest tendency to segregation of tungsten and molybdenum, and the lowest in the case of niobium.[35] At the same time, it should be noted that these values are lower than for analogous phenomena in nickel solid solution, which indicates a slower course of diffusion processes in nickel superalloys with the addition of these components.[36–38] The consequence of this observation is the conclusion that Co–Al–X cobalt superalloys with the addition of W, Mo and Nb require heat treatment with time and temperature parameters considering a slower diffusion course (chemical composition homogenization). However, the more important conclusion is the statement that thanks to this, the new cobalt superalloys will in principle behave more favorably in the conditions of thermally activated structural processes, e.g., under creep conditions, which is a great advantage over nickel superalloys.[39–41]

The last part of studies concerned macrostructure of the alloys. For this purpose, the series of micrographs were acquired and collected to one image (Figure 9). The micrographs were captured from the middle of ingot to outer edge to observe microstructural changes across the plane perpendicular to ingot axis. All alloys exhibit presence of very narrow or even lack of equiaxed crystals zone in the middle area. The thin chill zone may be observed in outer areas. However, all investigated alloys exhibit mostly elongated crystals, which are characteristic for fast solidification.

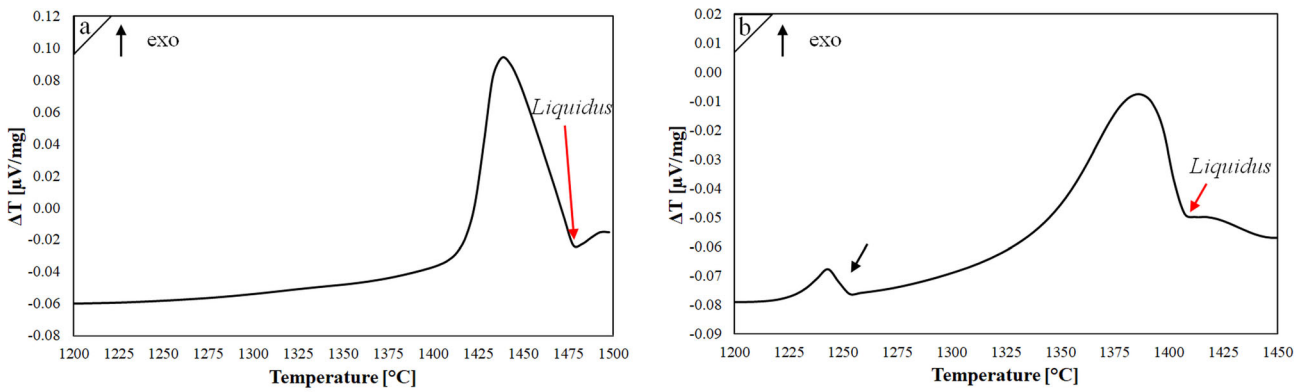

Figure 7. DTA cooling plots: (a) Co–9Al–9W; (b) Co–10Al–5Mo–2Nb.

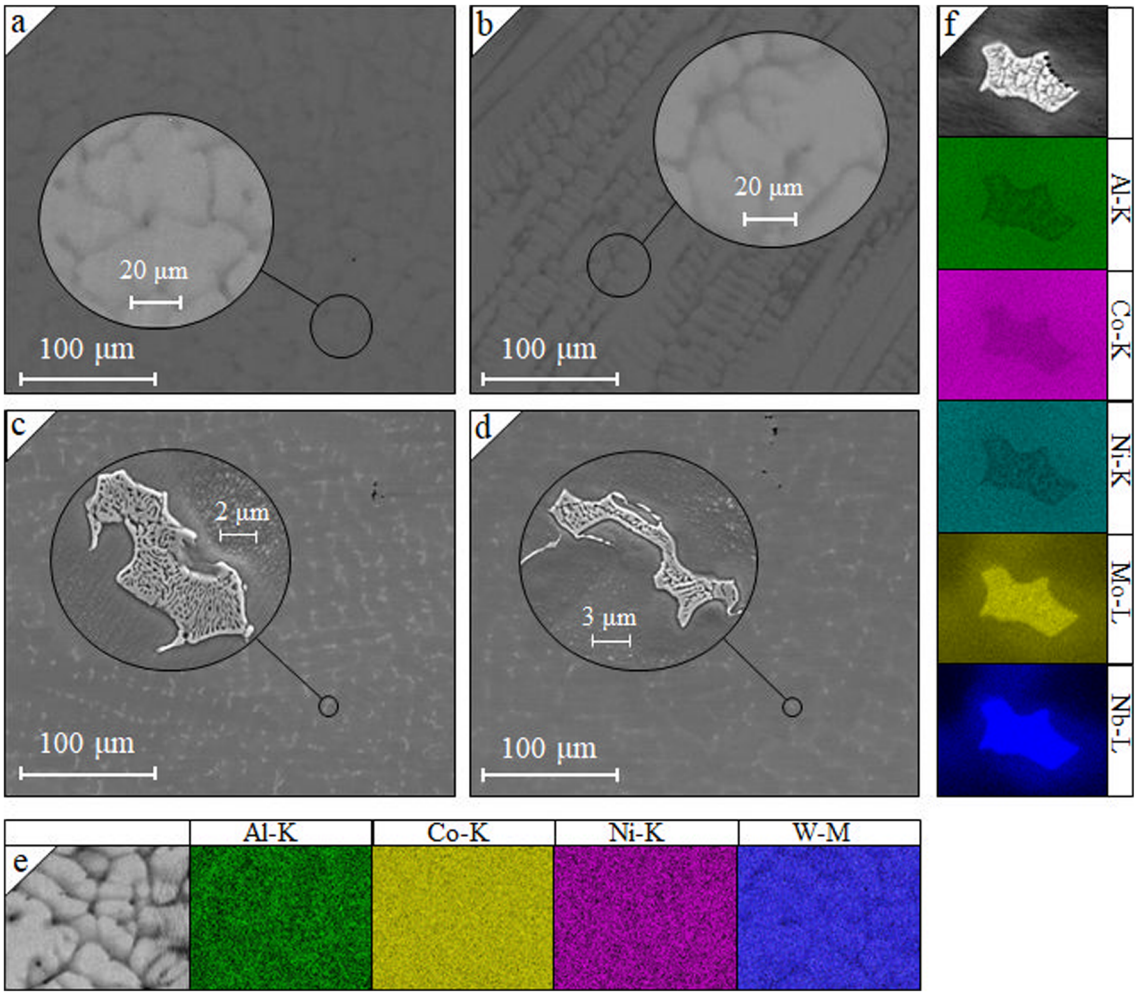

Figure 8. SEM micrographs of as-cast microstructure: (a) Co–9Al–9W; (b) Co-20Ni-7Al-7W; (c) Co-10Al-5Mo-2Nb; (d) Co-20Ni-10Al-5Mo-2Nb; (e) qualitative elemental mapping images of Al, Co, Ni, W corresponding to Co-20Ni-7Al-7W alloy; (f) qualitative elemental mapping images of Al, Co, Ni, Mo, Nb corresponding to Co-20Ni-10Al-5Mo-2Nb alloy.

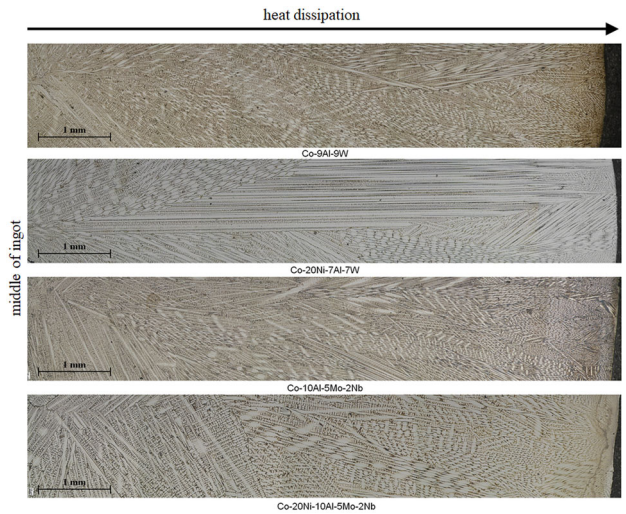

Figure 9. LM micrographs of primary microstructure of investigated alloys: plan view perpendicular to the ingot axis.

Conclusions

The γ–γ' type Co-based alloys are characterized by secondary dendrite arm spacings comparable to those of Ni-based superalloys.

The value of SDAS does not vary considerable within the compositions of the investigated Co-based alloys

W-free superalloys Co–(Ni)–Al–Mo–Nb are characterized by lower shrinkage porosity compared to that of Co–(Ni)–Al–W alloys.

The investigated Co-based alloys are characterized by a typical dendritic structure, composed of equiaxed and columnar crystals zones, and thin chill zone.

The W-free alloys are characterized by substantially higher solidification rate, which is caused by the presence of the

intermetallic phases rich in Mo and Nb, which crystallize at lower temperature compared to that of Co_{ss}.

Acknowledgments

This work was supported by National Science Centre (Project 2018/29/N/ST8/02062).

REFERENCES

1. J. Sato J, T. Omori, K. Oikawa, I. Ohnuma, R. Kainuma, K. Ishida, Cobalt-base high-temperature alloys, Science (2006) https://doi.org/10.1126/science.1121738
2. D. Coutsouradis, A. Davin, M. Lamberigts, Mater. Sci. Eng. (1987). https://doi.org/10.1016/0025-5416(87)90061-9
3. R.C. Reed The Superalloys, Fundamentals and Applications Cambridge University Press, Cambridge (2006)
4. C. Cui, D. Ping, Y. Gu, H. Harada, Mater. Trans. (2006). https://doi.org/10.2320/matertrans.47.2099
5. T.M. Pollock, J. Dibbern, M. Tsunekane, J. Zhu, A. Suzuki, JOM (2010). https://doi.org/10.1007/s11837-010-0013-y
6. K. Shinagawa, T. Omori, J. Sato, K. Oikawa, I. Ohnuma, R. Kainuma, K. Ishida, Mater. Trans. (2008). https://doi.org/10.2320/matertrans.MER2008073
7. G. Feng, H. Li, S.S. Li, J.B. Sha, Scr. Mater. (2012). https://doi.org/10.1016/j.scriptamat.2012.06.013
8. S.K. Makineni, B. Nithin, K. Chattopadhyay, Scr. Mater. (2015). https://doi.org/10.1016/j.scriptamat.2014.11.009
9. C.H. Zenk, I. Povstugar, R. Li, F. Rinaldi, S. Neumeier, D. Raabe, M. Göken, Acta Mater. (2017). https://doi.org/10.1016/j.actamat.2017.06.024
10. H.J. Im, S.K. Makineni, B. Gault, F. Stein, D. Raabe, P.-P. Choi, Scr. Mater. (2018). https://doi.org/10.1016/j.scriptamat.2018.05.041
11. P. Zhou, X. Gao, D. Song, Y. Liu, J. Cheng, Scanning (2021). https://doi.org/10.1155/2021/6678085
12. Y. Guan, Y. Liu, Z. Ma, H. Li, H. Yu, Vacuum (2020). https://doi.org/10.1016/j.vacuum.2020.109247
13. Y. Guan, Y. Liu, Z. Ma, H. Li, H. Yu, Investigation on γ' stability in CoNi-based superalloys during long-term aging at 900 °C. J. Alloy. Comp. (2020). https://doi.org/10.1016/j.jallcom.2020.155891
14. E. T. McDevitt, Vacuum induction melting and vacuum arc remelting of Co–Al–W-X gamma-prime superalloys. In: MATEC web of conferences (2014) https://doi.org/10.1051/matecconf/20141402001
15. S. Aliakbari Sani, H. Arabi, S. Kheirandish, G. R. Ebrahimi, Int. J. Min. Met. (2019) https://doi.org/10.1007/s12613-019-1727-7
16. A. Tomaszewska, T. Mikuszewski, G. Moskal, D. Migas, J. Alloy. Comp. (2018). https://doi.org/10.1016/j.jallcom.2018.03.397
17. X.Z. Zhou, H.D. Fu, Y. Zhang, H. Xu, J.X. Xie, J. Alloy. Compd. (2018). https://doi.org/10.1016/j.jallcom.2018.07.218
18. X.Z. Zhou, H.D. Fu, Y. Zhang, H. Xu, J.X. Xie, Adv. Eng. Mater. (2019). https://doi.org/10.1002/adem.201900641
19. J. Koßmann, C.H. Zenk, I. Lopez-Galilea, S. Neumeier, A. Kostka, S. Huth, W. Theisen, M. Göken, R. Drautz, T. Hammerschmidt, J. Mater. Sci. **50**, 6329–6338 (2015). https://doi.org/10.1007/s10853-015-9177-8
20. S.K. Makineni, A. Samanta, T. Rojhirunsakool, T. Alam, B. Nithin, A.K. Singh, R. Banerjee, K. Chattopadhyay, A new class of high strength high temperature cobalt based γ-γ' Co-Mo-Al alloys stabilized with Ta addition. Acta Mater. **97**, 29–40 (2015)
21. S.K. Makineni, B. Nithin, K. Chattopadhyay, Synthesis of a new tungsten-free γ-γ' cobalt-based superalloy by tuning alloying additions. Acta Mater. **85**, 85–94 (2015)
22. Q. Liu, J. Coakley, D.N. Seidman, D.C. Dunand, Precipitate evolution and creep behavior of a W-free Co-based superalloy. Metall. Mater. Transact. **47A**, 6090–6096 (2016)
23. K. Shinagawa, T. Omori, J. Sato, K. Oikawa, I. Ohnuma, R. Kainuma, K. Ishida, Phase equilibria and microstructure on γ' phase in Co–Ni–Al–W system. Mater. Trans. **49**, 1474–1479 (2008)
24. H.-Y. Yan, J. Coakley, V.A. Vorontsov, N.G. Jones, H.J. Stone, D. Dye, Alloying and the micromechanics of Co–Al–W–X quaternary alloys. Mater. Sci. Eng., A **613**, 201–208 (2014)
25. S. Neumeier, L.P. Freund, M. Göken, Novel wrought γ/γ' cobalt base superalloys with high strength and improved oxidation resistance. Scripta Mater. **109**, 104–107 (2015)
26. C. H. Zenk, S. Neumeier, N. M. Engl, S. G. Fries, O. Dolotko, M. Weiser, Sa. Virtanen, M. Göken, Intermediate Co/Ni-base model superalloys-thermophysical properties, creep and oxidation. Scripta Materialia 112(2016) 83–86.

27. A. Tomaszewska, T. Mikuszewski, G. Moskal, D. Migas, Primary microstructure, microsegregation and precipitates characterization of an as-cast new type γ-γ′ Co-Al-Mo-Nb cobalt-based superalloy. J. Alloy. Compd. **750**, 741–749 (2018). https://doi.org/10.1016/j.jallcom.2018.03.397
28. A. Tomaszewska, G. Moskal, D. Migas, M. Mikuśkiewicz, T. Maciąg, Thermal parameters determination of Co-Al-W as-cast alloy homogenization by DTA analysis. J. Therm. Anal. Calorim. **134**, 157–164 (2018). https://doi.org/10.1007/s10973-018-7431-4
29. D. Migas, G. Moskal, T. Maciąg, Thermal analysis of W-free Co-(Ni)-Al-Mo-Nb superalloys. J. Therm. Anal. Calorim. **142**, 149–156 (2020). https://doi.org/10.1007/s10973-020-09375-7
30. S. Roskosz, Pract. Metallogr. (2013). https://doi.org/10.3139/147.110214
31. D. Migas, P. Gradoń, T. Mikuszewski, G. Moskal (2020) https://doi.org/10.1007/s10973-020-10279-9
32. S. Makineni, B. Nithin, D. Palanisamy, K. Chattopadhyay, J. Mater. Sci. (2016). https://doi.org/10.1007/s10853-016-0026-1
33. S. Ida, R. Yamagata, H. Nakashima, S. Kobayashi, M. Takeyama, Phase equilibria among γ/TCP/GCP phases in Nb-poor region of Ni-Nb-Co ternary system at elevated temperatures. J. Ph. Equilibria Diffus. (2019). https://doi.org/10.1007/s11669-019-00744-w
34. D. Davydov, N. Kazantseva, N. Popov, N. Vinogradova, I. Ezhov, Phase transitions in the Co–Al–Nb–Mo system. Metals (2021). https://doi.org/10.3390/met11121887
35. S. Neumeier, H.U. Rehman, J. Neuner, C.H. Zenk, S. Michel, S. Schuwalow, J. Rogal, R. Drautz, M. Goken, Diffusion of solutes in fcc Cobalt investigated by diffusion couples and first principles kinetic Monte Carlo. Acta Mater. **106**, 304–312 (2016). https://doi.org/10.1016/j.actamat.2016.01.028
36. M.S.A. Karunaratne, P. Carter, R.C. Reed, Interdiffusion in the face-centred cubic phase of the Ni-Re, Ni-Ta and Ni-W systems between 900 and 1300 °C. Mater Sci. Eng. **281**, 229–233 (2000)
37. M.S.A. Karunaratne, R.C. Reed, Interdiffusion of niobium and molybdenum in nickel between 900–1300 °C, Defect Diffus. Forum **237–240**, 420–425 (2005)
38. M.S.A. Karunaratne, R.C. Reed, Interdiffusion of the platinum-group metals in Nickel at elevated temperatures. Acta Mater **51**, 2905–2919 (2003)
39. F. Qiu, K. Bu, J. Song, G.-L. Tian, X.-D. Zhang, Dimensional control of nickel-based single crystal turbine blade investment casting by process control optimization. Int. Metalcast. **12**, 469–479 (2018). https://doi.org/10.1007/s40962-017-0180-5
40. M.F. Moreira, L.B. Fantin, C.R.F. Azevedo, Microstructural characterization of Ni-base superalloy as-cast single crystal (CMSX-4). Inter Metalcast. **15**, 676–691 (2021). https://doi.org/10.1007/s40962-020-00496-1
41. D. Baker, W. Denning, G. Mirabelli, Effect of chemical composition and heat treatment on the corrosion resistance of cast nickel alloy C276. Int. J. Met. **9**, 76–77 (2015). https://doi.org/10.1007/BF03355606